




Angular dependence of Hall effect and magnetoresistance in SrRuO₃-SrIrO₃ heterostructuresSven Esser,¹ Jiongyao Wu,² Sebastian Esser,¹ Robert Gruhl,¹ Anton Jesche ¹ Vladimir Roddatis ^{3,4} Vasily Moshnyaga,⁵ Rossitza Pentcheva,² and Philipp Gegenwart ¹¹*Experimentalphysik VI, Center for Electronic Correlations and Magnetism, Augsburg University, D-86159 Augsburg, Germany*²*Department of Physics and Center for Nanointegration Duisburg-Essen (CENIDE), University of Duisburg-Essen, Lotharstr. 1, 47057 Duisburg, Germany*³*Institut für Materialphysik, Georg-August-Universität Göttingen, D-37077 Göttingen, Germany*⁴*GFZ German Research Centre for Geosciences, Telegrafenberg 14473, Potsdam, Germany*⁵*I. Physikalisches Institut, Georg-August-Universität Göttingen, D-37077 Göttingen, Germany*

(Received 9 September 2020; revised 23 March 2021; accepted 26 May 2021; published 21 June 2021)

The perovskite SrRuO₃ is a prototypical itinerant ferromagnet which allows interface engineering of its electronic and magnetic properties. We report the synthesis and investigation of atomically flat artificial multilayers of SrRuO₃ with the spin-orbit semimetal SrIrO₃ in combination with band-structure calculations with a Hubbard U term and topological analysis. The latter reveal an electronic reconstruction and emergence of flat Ru-4d_{xz} bands near the interface, ferromagnetic interlayer coupling, and a negative Berry-curvature contribution to the anomalous Hall effect. We analyze the Hall effect and magnetoresistance measurements as a function of the field angle from an out-of-plane towards an in-plane orientation (either parallel or perpendicular to the current direction) by a two-channel model. The magnetic easy direction is tilted by about 20° from the sample normal for low magnetic fields, rotating towards the out-of-plane direction by increasing fields. Fully strained epitaxial growth enables a strong anisotropy of magnetoresistance. An additional Hall effect contribution, not accounted for by the two-channel model, is compatible with stable skyrmions only up to a critical angle of roughly 45° from the sample normal. Within about 20° from the thin film plane an additional peaklike contribution to the Hall effect suggests the formation of a nontrivial spin structure.

DOI: [10.1103/PhysRevB.103.214430](https://doi.org/10.1103/PhysRevB.103.214430)**I. INTRODUCTION**

The demand for high-density and energy-efficient electronic devices has generated enormous interest in magnetic skyrmions, i.e., topologically protected spin textures [1], during the last decade [2,3]. For instance, controlled modification of skyrmion information may be utilized in energy-efficient racetrack memory devices [4]. Magnetic skyrmions can be generated by different mechanisms. For thin films a promising strategy is the combination of a ferromagnetic (FM) material with a strong spin-orbit coupled heavy metal, introducing a Dzyaloshinskii-Moriya interaction (DMI) at the interface due to the broken inversion symmetry [5].

Sharp inversion symmetry breaking interfaces can be grown in heterostructures of different perovskite oxides. Recently, Li *et al.* [6] showed, in bilayers of FM La_{0.7}Sr_{0.3}MnO₃ (LSMO) with the spin-orbit coupled semimetal SrIrO₃ (SIO) [7,8], the appearance of a giant topological Hall effect (THE), related to the LSMO/SIO interface. In thin film heterostructures composed of the FM metal SrRuO₃ (SRO) [9,10] and the ferroelectric BaTiO₃, Wang *et al.* [11] found a broken inversion symmetry at the interface due to the FE proximity effect, enabling electric control of the skyrmion properties.

The combination of SRO and SIO grown on a SrTiO₃ (STO) substrate offers an excellent possibility to obtain epitaxial thin heterostructures with multiple interfaces. Both

components crystallize in the same ABO₃-related perovskite structure as the substrate STO with similar valences at both the A and the B sites, avoiding charge accumulation and polar catastrophe at the interface [12]. Furthermore, their (pseudo)cubic lattice constants are rather similar, i.e., the lattice mismatch is smaller than 0.97%.

Matsuno *et al.* [13] reported the first suggestions of the presence of skyrmions in bilayers of 2-unit-cell (u.c.) SIO on 4- to 7-u.c. SRO (on an STO substrate) by analyzing an unconventional contribution to the Hall effect at temperatures below 100 K, which they interpreted as a THE. Resulting from a Berry phase in real space [14], the THE is a promising indicator of skyrmions, first demonstrated in MnSi [15].

For the inverted heterostructure, i.e., SRO (3–5 u.c.)–SIO (2 u.c.) on STO, the AHE and THE contributions were successfully varied by electric field tuning and the change in the THE was attributed to a change in size of the topological spin textures by modification of the DMI [16]. A similar THE was also observed in other studies on SRO-SIO superlattices (SLs) as well as in SRO films [17,18] and linked to the appearance of skyrmions [19,20]. By contrast, other groups did not relate the anomalies in the Hall signal to a topological contribution. Instead, they considered the anomalous Hall resistance due to different magnetic domains in SRO [21–23], the variation of the magnetic and electronic properties between individual SRO layers [24], thickness inhomogeneities in the SRO layers

[25], or defect-induced anomalies [26]. From tight-binding calculations Groenendijk *et al.* [27] arranged the electronic structure of SRO in groups of three bands, with two low-lying nontrivial bands with Chern number $C = \pm 2$. They describe the AHE effect phenomenologically by superposition of two channels arising from nontrivial Berry curvature in reciprocal space, although real-space Berry curvature effects due to non-collinear spin textures could not be excluded. Thus, further experimental characterization of the Hall effect in SRO-SIO systems is greatly needed to clarify the situation.

Below, we report a detailed combined study of density functional theory (DFT) including a Hubbard U term and spin orbit coupling (SOC) band-structure calculations and angular-dependent magnetotransport and Hall effect on $[(\text{SRO})_5/(\text{SIO})_2]_k$ (SROSIO) $_k$ ($k = 1-10$) multilayer thin films grown along the [001] direction. The latter were prepared by metalorganic aerosol deposition, which realizes an oxygen-rich growth atmosphere, ideal for high-quality perovskite oxide thin films [28–30]. The band structure of the superlattice displays dispersive and emergent flat bands near the interface. Analysis of the experimental data with a phenomenological two-band model successfully explains the overall transport properties. An additional Hall contribution can be associated with skyrmions only when the field is applied at an angle between 0 and 45° from the sample normal.

II. METHODS

Thin films of (SROSIO) $_k$ heterostructures were grown on (001)-oriented STO substrates by metalorganic aerosol deposition. The growth of each layer was monitored *in situ* by optical ellipsometry, which allows the resolution of variations on a monolayer length scale [31]. The film thickness was determined by x-ray reflectometry utilizing a Malvern Panalytical Empyrean diffractometer and subsequently simulated with REMAGX [32] software. Thereby the thickness of each layer and the interface roughness could be extracted. The crystal structure, phase purity, and strain state were determined by x-ray diffraction and reciprocal space mapping operating with Cu- $K_{\alpha 1}$ radiation by means of a hybrid monochromator.

The temperature- and magnetic-field-dependent magnetization was measured in a magnetic property measurement system (MPMS3) equipped with a 7-T magnet in a stabilized dc mode. To obtain the proper magnetization of the thin film the raw background signal of the substrate material was carefully subtracted in each measurement point from the raw measurement signal of the sample and analyzed afterwards by the standard procedure of the magnetic property measurement system. The temperature and magnetic field dependence of the electrical resistivity was determined in a physical property measurement system equipped with a 14-T magnet and an electrical transport option. Each thin film was microstructured with argon-ion etching in a standard Hall bar geometry. The angle-dependent magnetoresistance (MR) and Hall effect studies were performed with a physical property measurement system horizontal rotator.

Density functional theory [33] calculations were performed with the VASP [34] code with the PBEsol [35–37] exchange-correlation functional, which is known to improve the structural description of solids. Static local correlation

effects were considered within the DFT + U approach in the Dudarev implementation [38], using $U = 1.0$ eV for Ru [39]. For Ir we used $U = 1.37$ eV, $J = 0.22$ eV, obtained from linear response theory for the bulk compound [40]. We model the $(\text{SrRuO}_3)_n/(\text{SrIrO}_3)_2(001)$ SL by using laterally a $\sqrt{2}a \times \sqrt{2}a$ unit cell, with a set to the lattice constant of STO and two transition metal sites per layer to account for the octahedral rotations and tilts. Since an odd number of layers constrains the tilt pattern and the numerical demand for doubling the unit cell in the z direction for $n = 5$ is too high, we have performed additional calculations with $n = 4$ and for a $[(\text{SrRuO}_3)_3/(\text{SrIrO}_3)_2]_2(001)$ SL. Since the results for $n = 4$ and 5 were qualitatively very similar, we proceed here with the results for $n = 5$, which correspond to the experimental setup. A plane-wave cutoff energy of 500 eV was used. The calculations were performed with a Γ -centered k -point grid of $6 \times 6 \times 2$. The convergence criterion of the self-consistent calculation is 10^{-5} eV for the total energy. A Fermi level smearing of 0.05 eV is used for the geometry optimization and further analysis. The lattice parameter c and the internal coordinates of the structure were optimized until the atomic forces were less than 0.01 eV/Å. SOC was considered with the magnetization direction along the [001] and [100] quantization axes; below we report the results for the [001] orientation. The DFT + U + SOC band structure was fitted to maximally localized Wannier functions using the WANNIER90 code [41] and the Berry curvature and anomalous Hall conductivity were calculated on a dense k -point mesh of $100 \times 100 \times 10$.

III. RESULTS

A. Structural investigations

X-ray diffraction measurements [Fig. 1(a)] on (001) $_{\text{pc}}$ -oriented SROSIO thin films on (001)-oriented STO substrates indicate out-of-plane epitaxial growth. The measured pseudocubic out-of-plane lattice constant $d_{\text{pc}} = 3.950(4)$ Å is slightly larger than that of bulk SRO ($d_{\text{SRO}} = 3.923$ Å) [42] and SIO ($d_{\text{SIO}} = 3.942$ Å) [43]. This can be explained by the compressive in-plane strain of $\sim 0.44\%$ and $\sim 0.97\%$ due to the lattice mismatch for SRO/STO and SIO/STO, respectively. Reciprocal space mapping around the (103)-STO peak [Fig. 1(c)] confirms the fully strained state of the film. The occurrence of Laue fringes in the x-ray diffraction pattern (see Supplemental Material [44]) indicates the high quality of our films. Small-angle x-ray reflectometry measurements indicate a large-scale homogeneity for the growth of each SRO and SIO layer independently. This homogeneous growth is in good agreement with the measured time dependence of the imaginary part of the reflection coefficients during the synthesis, plotted in Fig. 2. As shown previously [31,49], for ultrathin films of a thickness smaller than the wavelength, the phase shift detected by ellipsometry increases linearly with the thickness, with a slope that depends on the material's optical constants and thus changes between the different layers. Thus, the heterostructure growth is clearly visible in the time-dependent signal.

B. Band-structure calculations

The DFT + U + SOC calculations show that bulk SRO is half-metallic with a spin and orbital magnetic moment of

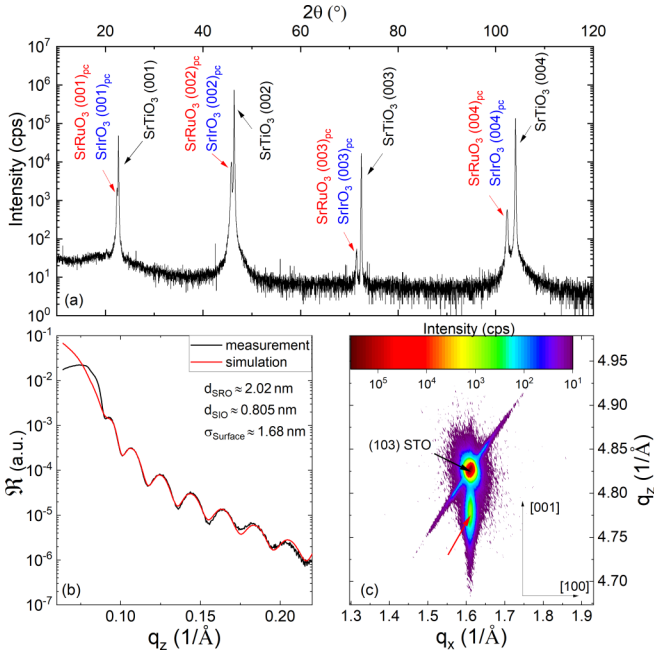


FIG. 1. (a) θ - 2θ x-ray diffraction scan: Black arrows indicate peaks of the (001)-STO substrate, whereas red arrows mark peaks of (001)_{pc}-SRO and (001)_{pc}-SIO. (b) X-ray reflectometry measurement of a [(SRO)₅/(SIO)₂]₁₀ heterostructure including the simulation with REMAGX [32]. (c) Reciprocal space map around the (103) peak of STO (black arrow) indicating the fully strained state of the heterostructure marked by the red arrow.

$1.39\mu_B$ and $0.03\mu_B$, respectively, and SIO is a semimetal with quenched spin and orbital moments, consistent with previous studies [40,50]. In Fig. 3 we show a side view of the spin density (with FM interlayer coupling) and the layer-resolved density of states of the (SrRuO₃)₅/(SrIrO₃)₂(001) SL from

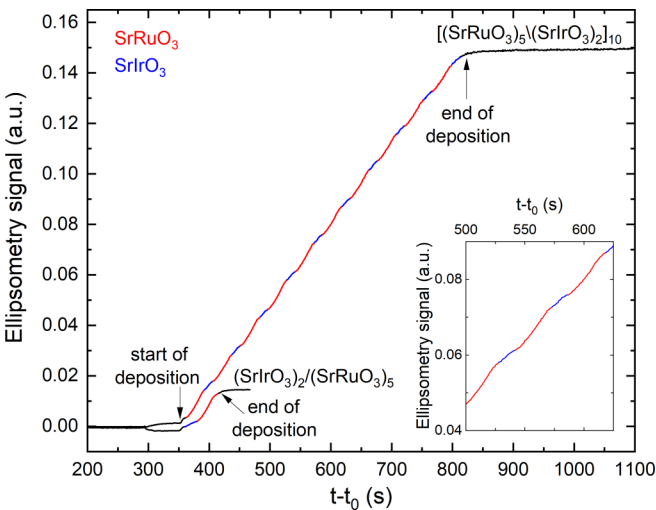


FIG. 2. Ellipsometry signal as a function of time during the growth of a (SrIrO₃)₂/(SrRuO₃)₅ bilayer structure and a 10 times repeated bilayer structure [(SrRuO₃)₅/(SrIrO₃)₂]₁₀. Black arrows indicate the start and the end of the deposition. The measured signals during the growth of SRO and SIO are shown in red and blue, respectively.

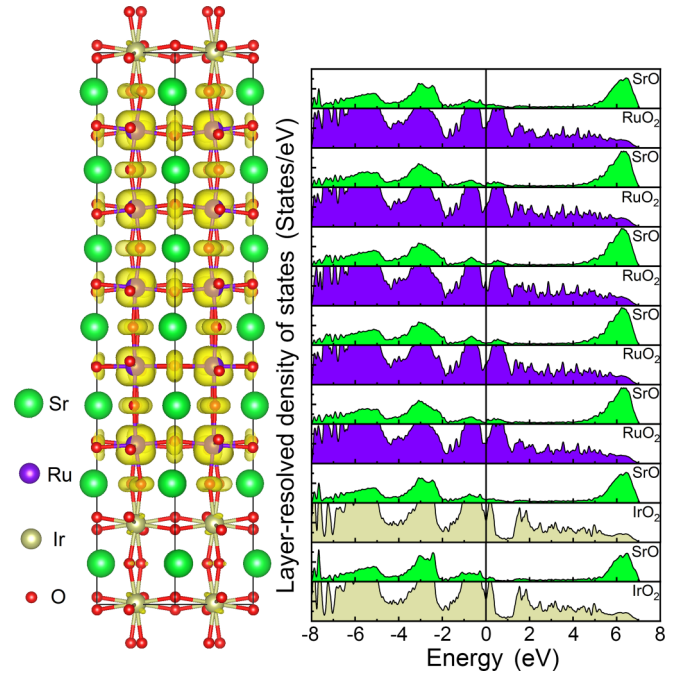


FIG. 3. Side view of the spin density (left) and layer-resolved density of states (LDOS; right) of the (SrRuO₃)₅/(SrIrO₃)₂(001) SL with SOC along [001]. Zero energy in the LDOS denotes the Fermi level. Note that the magnetic coupling between the SRO blocks along the z direction is ferromagnetic; see the text.

the DFT + U + SOC calculation with magnetization along the [001] direction. The layer-resolved density of states shows metallic behavior (note that SOC formally entangles the two spin directions, nevertheless, the predominance of majority spin states at the Fermi level is preserved) in both the SRO and the SIO parts of the SL with a dip in the density of states at the Fermi level.

Concerning the magnetic properties, the spin and orbital moments at the Ru sites in the inner part of the SRO region are $\sim 1.41\mu_B$ and $0.05\mu_B$, respectively, whereas a slight reduction occurs at the interface, $\sim 1.38\mu_B$ and $0.02\mu_B$. In contrast to bulk SIO, in the SRO/SIO SL a finite spin and orbital moment are induced at the Ir sites of 0.09 and $0.04\mu_B$, respectively, emphasizing the electronic and magnetic reconstruction in this system. The spin density in Fig. 3 illustrates the t_{2g} orbital character at the Ru sites, as well as a notable contribution from the oxygen sites indicating substantial covalency of the bond in the SRO part, whereas the spin density is nearly quenched in the SIO part. We have performed calculations for a [(SrRuO₃)₃/(SrIrO₃)₂]₂(001) SL with a ferro- and antiferromagnetic arrangement of the two SRO parts. Our results indicate that the FM coupling between the SRO blocks through SIO is strongly favored by ~ 0.652 eV per simulation cell.

More insight into the electronic properties and origin of the electronic reconstruction in the (SrRuO₃)₅/(SrIrO₃)₂(001) SL can be obtained from the band structure plotted in Fig. 4, which also indicates the layer-resolved orbital character. The band structure shows multiple bands crossing the Fermi level, dispersive ones of predominantly d_{xy} character in both the SIO

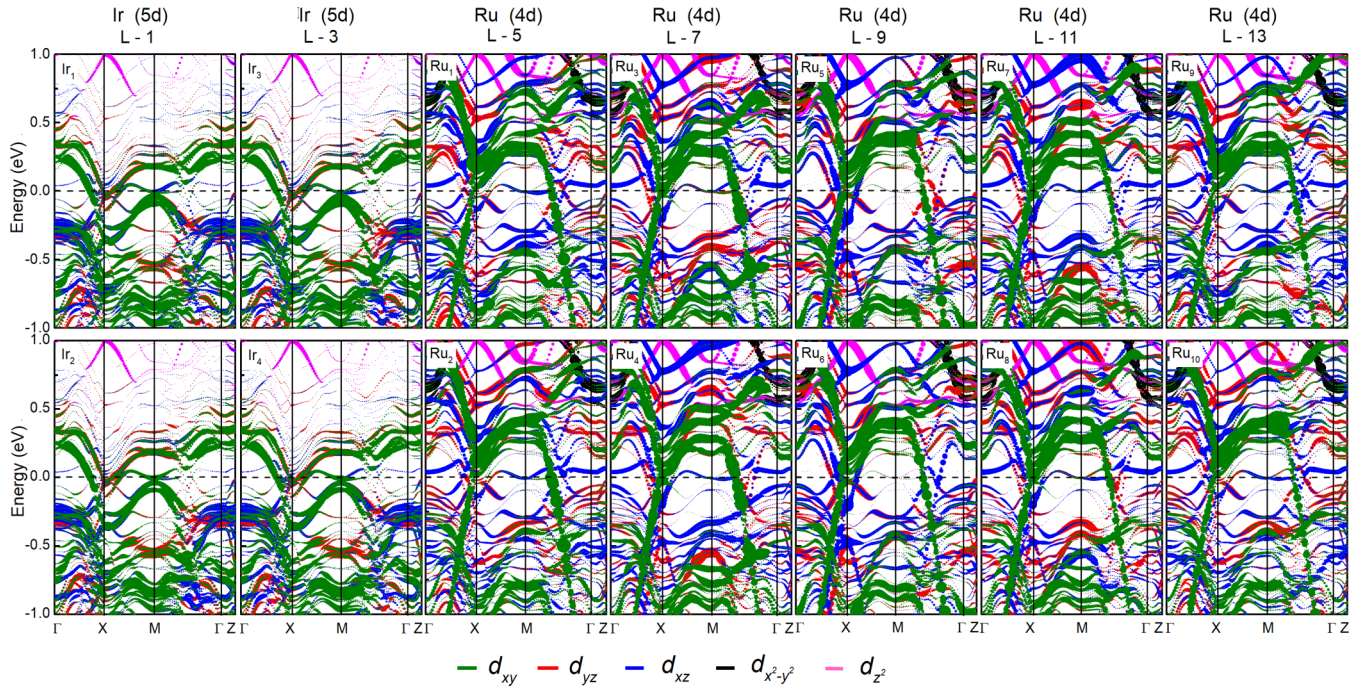


FIG. 4. Band structures of $(\text{SrRuO}_3)_5/(\text{SrIrO}_3)_2(001)$ showing the contribution of Ir $5d$ and Ru $4d$ orbitals in different layers. Green, red, blue, black, and magenta curves denote d_{xy} , d_{yz} , d_{xz} , $d_{x^2-y^2}$, and d_{z^2} orbitals, respectively.

and the SRO part and flatter ones of d_{xz} character in the SRO part, in particular, in the interface region.

The band structures including SOC with out-of-plane magnetization of the end member SRO and the $(\text{SrRuO}_3)_5/(\text{SrIrO}_3)_2(001)$ SL are displayed in Figs. 5(a) and 5(b). The band structure of bulk SRO contains multiple bands crossing at E_F , with both electron- and holelike behavior as

a function of the energy (in units of e^2/h). Some features of the SRO bulk band structure are visible also in the SL with layer-dependent offsets and superimposed SIO contribution. By fitting the band structure to a tight-binding model with Wannier orbitals using the WANNIER90 code [41], we have furthermore calculated the Berry curvature [Fig. 5(c)] and [Fig. 5(b)] and anomalous Hall conductivity [Fig. 5(e)] and [Fig. 5(f)] of the two systems. The largest contribution to the Berry curvature $\Omega(k)$ arises between Γ and X in bulk SrRuO_3 and along X - M in $(\text{SrRuO}_3)_5/(\text{SrIrO}_3)_2(001)$. Overall this leads to a notable anomalous Hall conductivity exhibiting sign reversals as a function of the chemical potential. While at the Fermi level the anomalous Hall conductivity of SrRuO_3 is nearly quenched, it is negative for the $(\text{SrRuO}_3)_5/(\text{SrIrO}_3)_2(001)$ SL. As shown in Sec. III D, this is consistent with the experimental data below 80 K.

C. Magnetization

To investigate the magnetic anisotropy we applied the external magnetic field perpendicular (out-of-plane) and parallel (in-plane) to the film surface. Corresponding $M(H)$ and $M(T)$ curves are shown in Fig. 6(a). For magnetic fields oriented perpendicular to the film surface the magnetization is 3 times larger than for a field of the same magnitude lying in the film plane, indicating an out-of-plane anisotropy of the SROSIO heterostructures.

To investigate the influence of the number of interfaces we measured temperature-dependent magnetization curves for $[(\text{SRO})_5/(\text{SIO})_2]_k$ thin films with different repetitions k of the bilayer structure in an in-plane-oriented magnetic field of $\mu_0 H = 500$ Oe. As the magnetic reference signal we used a pure SRO thin film. In Fig. 6(b) the obtained $M(T)$ curves are shown. Compared to the SRO reference all SROSIO

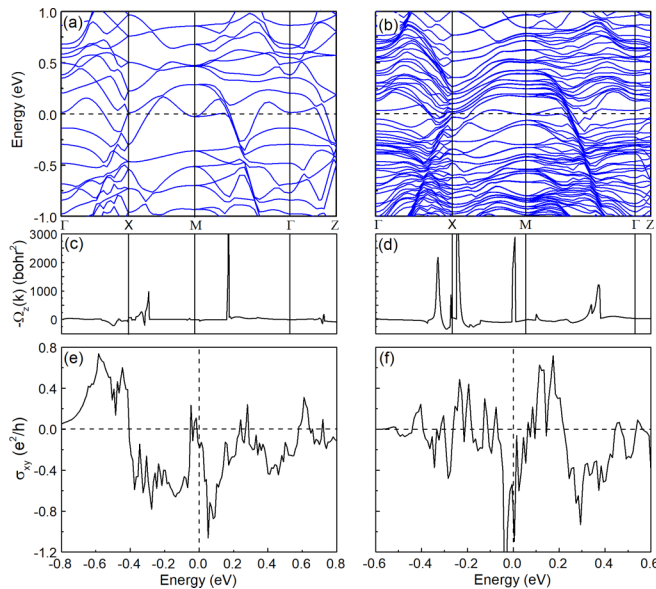


FIG. 5. Band structures of (a) bulk SrRuO_3 and (b) $(\text{SrRuO}_3)_5/(\text{SrIrO}_3)_2(001)$ with SOC with magnetization along the $[001]$ direction. (c, d) The Berry curvatures plotted along the same k path, and (e, f) the corresponding anomalous Hall conductivity σ_{xy} as a function of the energy (in units of e^2/h).

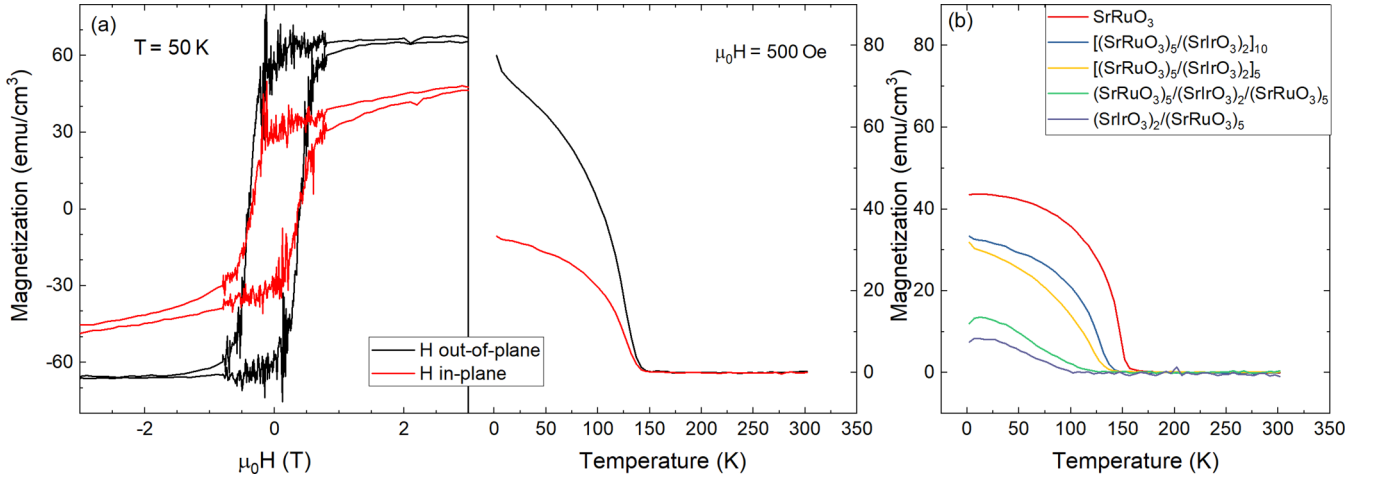


FIG. 6. Temperature- and magnetic-field-dependent magnetization of the SROSIO heterostructures. (a) $M(H)$ and $M(T)$ curves for a $[(\text{SRO})_5/(\text{SIO})_2]_{10}$ heterostructure with an external magnetic field oriented out-of-plane (black curve) and in-plane (red curve) with respect to the film surface. The difference in coercitive field indicates a magnetic easy axis oriented out-of-plane. (b) Temperature-dependent magnetization of different $[(\text{SRO})_5/(\text{SIO})_2]_k$ heterostructures measured in an in-plane magnetic field orientation. The magnetization of a pure SRO sample is added for comparison.

heterostructures have a smaller magnetization and a lower ordering temperature T_C .

This can be explained by taking into account the ordering of the spins close to the interface. Due to the broken inversion symmetry between SRO and SIO a DMI results, which forces the spins in a noncollinear structure [51,52]. For most of the SRO layers, which are sandwiched symmetrically by SIO layers on top and bottom, the DMI has the same strength but opposite signs at the top and bottom. Thus, for magnetic fields perpendicular to the interface their effect cancels out and the magnetic moments of those SRO layers align ferromagnetically as in a pure SRO thin film. However, for SRO layers with just one interface to SIO, such as the first layer grown directly on the STO substrate and the last top SRO layer for the sample with only one SIO layer between two SRO layers, the DMI does not cancel and the spins align in a noncollinear spin structure. For SROSIO heterostructures this means that in heterostructures with $k > 1$ repetitions $(k - 1)$ SRO layers order like a pure SRO thin film. With increasing k values the ordering temperature T_C of the heterostructure therefore approaches that of the pure SRO (see Table I).

In an in-plane-oriented magnetic field the spins order at the top and bottom interfaces in a conical phase with an opposite rotation sense. Due to the rotation of the moments the

magnetization parallel to the film plane is reduced compared to that of a pure SRO film. For example, the bilayer with five monolayers of SRO has the same T_C as four monolayers of a pure SRO thin film [10].

D. Magnetotransport

1. Temperature-dependent Hall effect and magnetoresistance

To investigate the magnetotransport properties of our heterostructures we applied an external magnetic field in the out-of-plane direction and measured both the Hall resistance, ρ_{xy} (transversal to current j), and the isothermal magnetoresistance, $\text{MR} = (\rho_{xx}(H) - \rho_{xx}(0))/\rho_{xx}(0)$ (parallel to j). The contribution of the ordinary Hall effect was determined by a linear fit in the high-field regimes ($|\mu_0 H| > 4$ T) and subtracted from the total Hall resistance. As shown in Figs. 7(a)–7(c) the anomalous Hall effect (AHE) changes sign between $T = 60$ K and $T = 80$ K. This sign change is known for SrRuO₃ and was related to a band-structure effect [53].

The shape of the AHE can be described by a phenomenological model with two AHE contributions,

$$\rho_{\text{AHE}} \propto \rho_{s1} \cdot \tanh\left(\frac{H - H_{c1}}{H_{s1}}\right) + \rho_{s2} \cdot \tanh\left(\frac{H - H_{c2}}{H_{s2}}\right),$$

introduced in [27] and [48]. In Fig. 8 this two-channel model is fitted to the Hall effect at $T = 10$ K. Here, both AHE contributions have similar signs but different sizes and coercitive fields (cf. the lower inset).

The upper inset shows the difference $\Delta\rho_{\text{Hall}} = \rho_{\text{Data}} - \rho_{\text{Fit}}$ between the experimental data and the fit with the two-channel model. A maximal value of $\Delta\rho_{\text{Hall}} = \pm 0.29 \mu\Omega \text{ cm}$ is found at $\mu_0 H \sim \pm 0.121$ T. This additional contribution $\Delta\rho_{\text{Hall}}$ to the total Hall effect may hint at a topological Hall effect in our heterostructures (see below). The temperature dependence of the coercitive fields H_{c1} and H_{c2} obtained from the fits by the two-channel AHE function is listed in the Supplemental Material [44].

TABLE I. Magnetic ordering temperature T_C of $[(\text{SRO})_5/(\text{SIO})_2]_k$ heterostructures with different numbers of interfaces in comparison with that of a pure 42-monolayer-thick SrRuO₃ thin film.

Sample	No. of interfaces	T_C (K)
SrRuO ₃	—	157
$[(\text{SrRuO}_3)_5/(\text{SrIrO}_3)_2]_{10}$	19	145
$[(\text{SrRuO}_3)_5/(\text{SrIrO}_3)_2]_5$	9	137
$(\text{SrRuO}_3)_5/(\text{SrIrO}_3)_2/(\text{SrRuO}_3)_5$	2	126
$(\text{SrIrO}_3)_2/(\text{SrRuO}_3)_5$	1	102

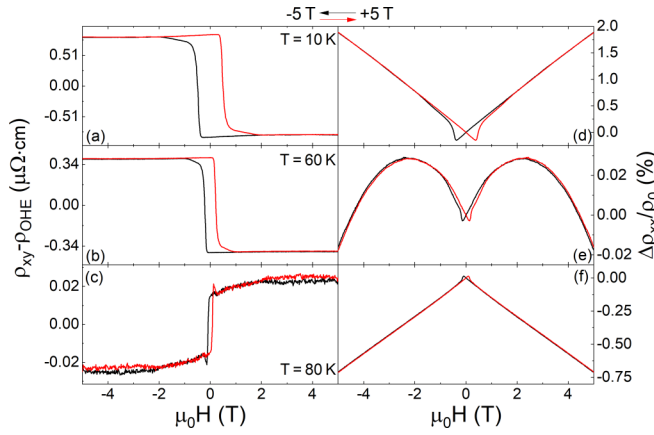


FIG. 7. (a–c) Hall effect and (d–f) isothermal magnetoresistance at various temperatures for a $[(\text{SRO})_5/(\text{SIO})_2]_{10}$ heterostructure measured in an out-of-plane-oriented external magnetic field. Black lines indicate magnetic field sweeps from +5 to –5 T, and red lines the opposite sweep direction. For the Hall resistance the contribution of the ordinary Hall effect was subtracted.

For different temperatures the magnetic field dependence of the absolute value of this extra contribution $\Delta\rho_{\text{Hall}}$ is shown in Fig. 9. We observe a shift of the maximum from $\mu_0 H \sim 0.4$ T at $T = 10$ K to $\mu_0 H \sim 0.12$ T at $T = 80$ K and a decrease from $\Delta\rho_{\text{Hall}} = 0.29 \mu\Omega\text{cm}$ to $\Delta\rho_{\text{Hall}} = 0.016 \mu\Omega\text{cm}$. For temperatures above $T \geq 90$ K $\Delta\rho_{\text{Hall}}$ vanishes.

We denote the field at which the absolute value of the additional Hall contribution is maximal H_{sk} . The latter is located close to the coercitive field H_{c1} at all temperatures below 90 K. The temperature dependence of the maximal absolute size of $\Delta\rho_{\text{Hall}}$ is shown in the inset in Fig. 9.

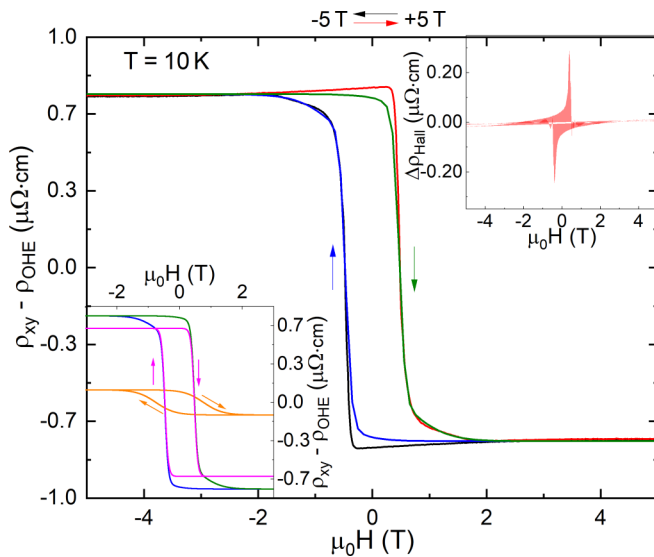


FIG. 8. Hall effect of a $[(\text{SRO})_5/(\text{SIO})_2]_{10}$ heterostructure (black and red lines) and the adjusted two-channel AHE model (blue and green lines) at $T = 10$ K. Lower inset: Contributions of both channels. Upper inset: Difference $\Delta\rho_{\text{Hall}} = \rho_{\text{Data}} - \rho_{\text{Fit}}$ between experiment and fit.

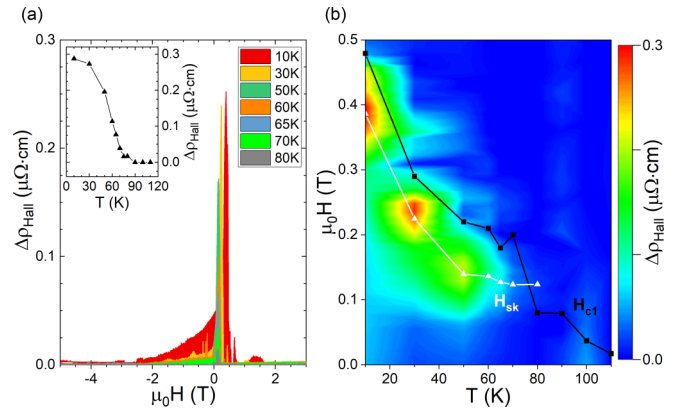


FIG. 9. Magnetic field dependence of $\Delta\rho_{\text{Hall}}$ (see text) of a $[(\text{SRO})_5/(\text{SIO})_2]_{10}$ heterostructure for temperatures $10 \text{ K} \leq T \leq 80 \text{ K}$. Inset: Temperature dependence of the maximal absolute value of $\Delta\rho_{\text{Hall}}$. (b) Color map of $\Delta\rho_{\text{Hall}}$ in the T - H plane. Black squares and white triangles denote the coercitive field (H_{c1}) and the field (H_{sk}) at which the additional contribution $\Delta\rho_{\text{Hall}}$ reaches its maximum, respectively.

Before analyzing the Hall effect and its angular dependence further, we turn to the magnetoresistance. The temperature-dependent MR [Figs. 7(d)–7(f)] can be separated into two ranges. At low temperatures ($T = 10$ K) the low-field MR is negative and becomes positive at higher magnetic fields, whereas it looks opposite at higher temperatures ($T = 80$ K). The crossover between the two types of dependences is located at $T = 60$ K.

For modeling the MR we can also use a two-channel model,

$$\frac{\Delta\rho_{xx}}{\rho_0} \propto A \left[H + M_{s1} \cdot \tanh\left(\frac{H - H_{c1}}{H_{s1}}\right) \right]^2 + C \left[H + M_{s2} \cdot \tanh\left(\frac{H - H_{c2}}{H_{s2}}\right) \right]^2, \quad (1)$$

with two additive contributions [44]. As shown in Fig. 10 the experimentally obtained MR can be well described by this

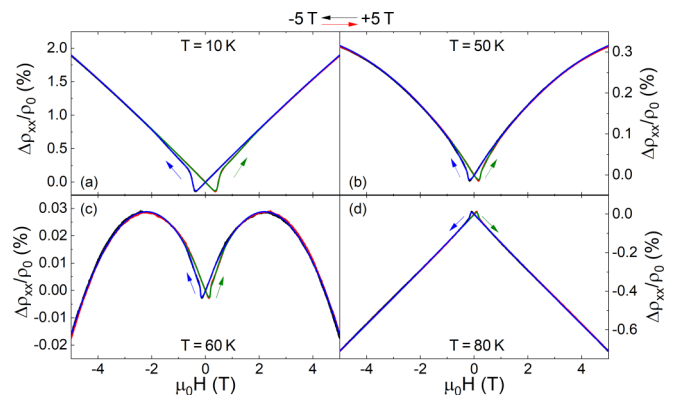


FIG. 10. Out-of-plane MR (black and red lines) and two-channel MR model (blue and green lines) of a $[(\text{SRO})_5/(\text{SIO})_2]_{10}$ heterostructure for $T = 10$ K (a), 50 K (b), 60 K (c), and 80 K (d).

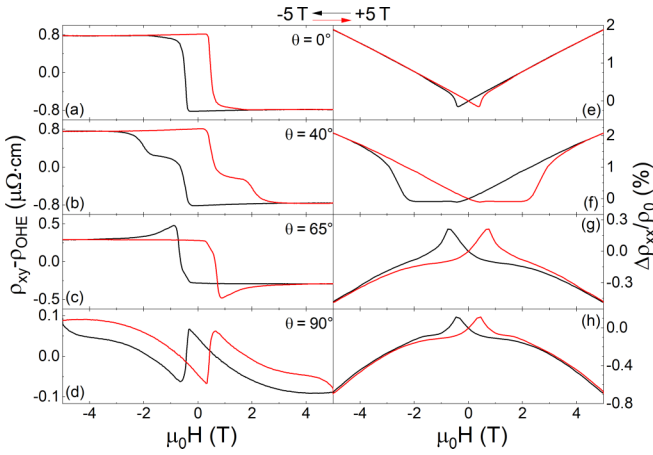


FIG. 11. (a–d) Hall effect and (e–h) MR of a $[(\text{SRO})_5/(\text{SIO})_2]_{10}$ heterostructure for various field angles θ from the sample normal to the in-plane direction parallel to the current at $T = 10$ K.

two-channel model, where the two channels have the same coercive fields H_{ci} as used for the fits of the AHE.

2. Field-angle-dependent Hall effect and magnetoresistance

Study of the angular dependence of the Hall effect (Fig. 11), in particular, its additional contribution $\Delta\rho_{\text{Hall}}$ discussed above, enables investigation of the stability of the assumed skyrmion structure. In our experiments the magnetic field was tilted in two different perpendicular arrangements from out-of-plane towards the in-plane direction. When the in-plane component ($H_{\text{in-plane}}$) of the magnetic field is tilted parallel to the current j the angle is labeled θ , whereas we use β as the tilt angle for the direction with both $H_{\text{in-plane}}$ and $H_{\text{out-of-plane}}$ perpendicular to j (cf. the sketch in Fig. S6 of the Supplemental Material [44]). For the out-of-plane direction, as described in Sec. III D 1, $\theta = 0^\circ$ and $\beta = 0^\circ$. Comparing both directions one finds similar shapes of the Hall effect except for angles near 90° , where the external magnetic field lies in the film plane. In particular, the ordinary Hall constant R_0 is similar for both tilt angles (see the Supplemental Material [44]), indicating that it is determined by the normal field component.

Similarly as above, we fit the AHE at various tilt angles β by the two-channel anomalous Hall effect model (cf. Fig. 12). For low angles, up to $\beta = 35^\circ$, both channels contribute with similar sign, while for $\beta = 55^\circ$ they have opposite signs, producing a strong humplike feature in ρ_{AHE} . The insets in Fig. 12 display the additional contribution $\Delta\rho_{\text{Hall}}$, whose field dependence, as discussed below, can be used to analyze the stability of possible interface skyrmions.

We note that the Hall effect of a pure SRO thin film demonstrates a weaker dependence of the field angle compared to the $(\text{SRO})_5/(\text{SIO})_{10}$ heterostructure (Fig. 13). Furthermore, the Hall effect of SRO can be consistently described by the two-channel AHE model (cf. Kim *et al.* [54] and Supplemental Material [44]) without any additional contribution. Thus, $\Delta\rho_{\text{Hall}}$ must be related to the interface between SRO and SIO. Comparing $\Delta\rho_{\text{Hall}}$ for all measured angles β we observe the expected “180° symmetry”, as demonstrated in Figs. 14(a) and 14(b).

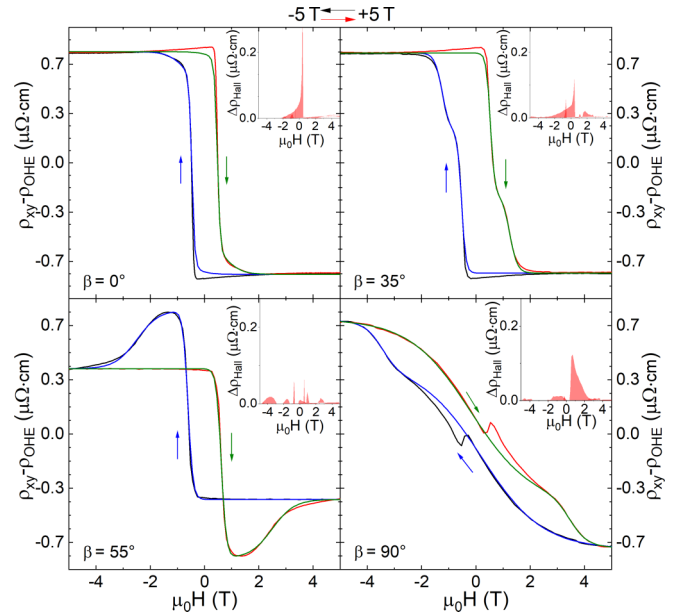


FIG. 12. Hall effect of a $[(\text{SRO})_5/(\text{SIO})_2]_{10}$ heterostructure after subtraction of the normal contribution for various field angles β from the sample normal to the in-plane direction perpendicular to the current (black and red lines) as well as fits by the two-channel model (see the text), indicated by blue and green lines. Inset: Difference $\Delta\rho_{\text{Hall}}$ between data and fit (see the text).

Assuming a THE due to skyrmions as the origin of the $\Delta\rho_{\text{Hall}}$, we now analyze its angular dependence. For Bloch-type skyrmions in MnSi thin films, Yokouchi *et al.* [55] found a stable skyrmion region for a film thickness d smaller than the helix length λ . The expected behavior of interface Néel-type skyrmions in a tilted magnetic field is different. While Bloch skyrmions coalign their axis with the direction of the tilted magnetic field, Néel skyrmions lock their symmetry axis to the high-symmetry direction of the thin film (perpendicular to the interface), leading to a deformation of the in-plane component ($H_{\text{in-plane}}$) of the magnetic field and thus an increase in their size [56].

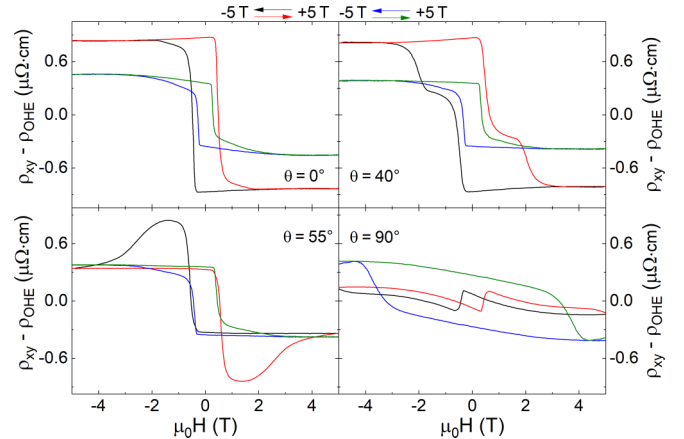


FIG. 13. Comparison of the angle-dependent Hall effect between $[(\text{SRO})_5/(\text{SIO})_2]_{10}$ (black and red curves) and pure SRO thin films (blue and green curves) for different tilt angles θ .

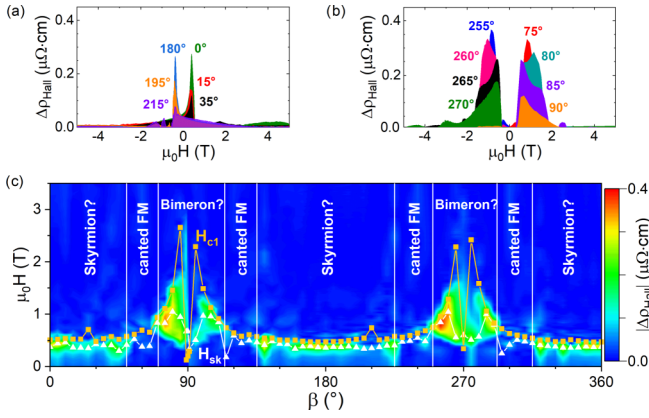


FIG. 14. Additional contribution $\Delta\rho_{\text{Hall}}$ (cf. Fig. 14) at 10 K for different magnetic field angles β as indicated by (a) and (b), close to the film normal and the in-plane field orientation, respectively. (c) Color map of $\Delta\rho_{\text{Hall}}$ in the β - H plane, which includes possible Néel skyrmions (skyrmion), the canted ferromagnetic phase (canted FM), and possible bimerons.

Since the magnitude of the THE is inversely proportional to the skyrmion cross section [5,16], an increasing skyrmion size is expected to lead to a decreasing THE. Importantly, we observe, for increasing field angles within 45° from the sample normal [cf. Fig. 14(a)], that the additional Hall contribution indeed shows a decreasing peak size. This is a remarkable result and supports the interpretation of the $\Delta\rho_{\text{Hall}}$ contribution as a THE arising from skyrmions. Outside these regimes, the strong increase in the calculated r_{sk} indicates that interface skyrmions become unstable. In a range of $\pm 20^\circ$ around the in-plane field orientation ($\beta = 90^\circ$ and $\beta = 270^\circ$) an unexpected peaklike structure appears in the Hall effect close to the coercitive field H_{c1} (Fig. 15). This structure could suggest a nontrivial spin structure different from that of Néel-type skyrmions (e.g., magnetic bimerons [57,58] or magnetic bubbles [59]).

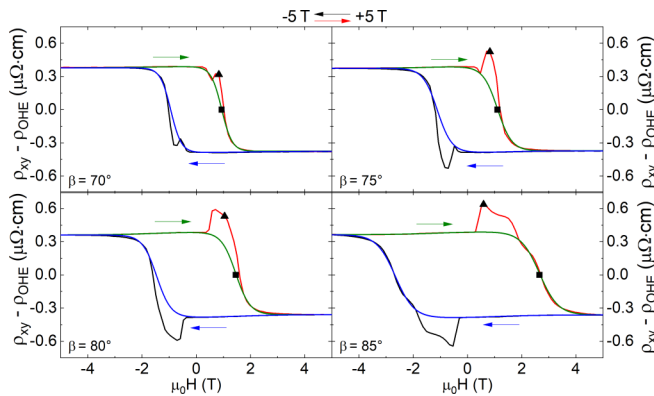


FIG. 15. Hall effect of a $[(\text{SRO})_5/(\text{SIO})_2]_{10}$ heterostructure (black and red lines) and the adjusted two-channel AHE model (blue and green lines) at $T = 10$ K for field orientations close to an in-plane direction. Note the additional peaklike structure, which cannot be modeled by the two-channel AHE model. Squares and triangles denote values of the coercive field (H_{c1}) and the field (H_{sk}) at which the additional contribution $\Delta\rho_{\text{Hall}}$ reaches its maximum, respectively.

As shown in Fig. 16, the MR at 10 K for tilting the magnetic field parallel to the current [tilt angle θ ; Figs. 16(a)–16(d)], as well as perpendicular to the current [tilt angle β ; Figs. 16(e)–16(h)] can always be well described by the two-channel MR model. In the former case, a crossover from positive MR for small θ to negative MR at large fields for large θ can be observed [cf. also Figs. 11(e)–11(h)]. The negative longitudinal magnetoresistance (LMR) could suggest the manifestation of Weyl fermions due to a chiral imbalance, as observed by Takiguchi *et al.* [60] in high-quality SRO thin films. Microscopic disorder, for example, interface roughness, could also lead to a negative LMR [61]. When tilting the magnetic field perpendicular to the current (tilt angle β) the MR shows a completely different behavior [see Figs. 16(e)–16(h)]. No crossover from positive to negative MR appears. Instead the positive MR value at ± 5 T increases and the hysteresis at smaller field values decreases from the out-of-plane to the in-plane direction.

For measuring the angle-dependent MR in a constant magnetic field, $1 \text{ T} \leq \mu_0 H \leq 5 \text{ T}$, the magnetization is first aligned parallel to the external field at 5 T in an out-of-plane direction. Afterwards the sample is rotated in the plane parallel (θ) and perpendicular (β) to the current measuring ρ_{xx} and ρ_{xy} .

For a magnetic field rotation perpendicular to the current direction [see Figs. 17(b) and 17(c)] a shift of the symmetry axis of the magnetization in the MR and Hall resistivity between $\mu_0 H = 1 \text{ T}$ and $\mu_0 H = 5 \text{ T}$ can be observed. The theoretical description of the angle-dependent magnetotransport properties in a constant magnetic field was done using a model introduced by Limmer *et al.* [62]. At high fields, $\mu_0 H \geq 4 \text{ T}$, the symmetry axis is aligned parallel to the out-of-plane direction of the sample, whereas it is tilted up to 20° from out-of-plane for low fields. Comparing both tilt directions we observe only a small variation of the angle-dependent MR for the magnetic field rotation perpendicular to the current, in contrast to the larger variation for tilting parallel to the current. The positive transversal magnetoresistance (TMR) which is measured for field rotation perpendicular to the current [cf. Figs. 16(e)–16(h)] displays only a small dependence on the magnetic field for in-plane and out-of-plane orientations. For $\theta = 90^\circ$ the magnetic and electric fields are in line, i.e., for this configuration the data represent the LMR, which is negative in our $(\text{SRO})_{10}$ heterostructure for magnetic fields $|\mu_0 H| \geq 2 \text{ T}$.

From the MR curves at $\theta = 0^\circ$, $\theta = 90^\circ$ and $\beta = 90^\circ$ one can calculate the anisotropic magnetoresistance (AMR) using the definition from [63]. The field dependence of the AMR at 10 K is shown in Fig. 18. Both the out-of-plane and the in-plane AMR is negative, whereas the in-plane AMR is larger than the out-of-plane AMR. The in-plane AMR specifies the ratio between the LMR ($\theta = 90^\circ$) and the in-plane TMR ($\beta = 90^\circ$), while the out-of-plane AMR is given by the ratio between the LMR and the out-of-plane TMR ($\theta = 0^\circ$). Both the in-plane and the out-of-plane TMR is larger than the LMR as indicated by the negative AMR ratio. The difference between both AMR ratios is related to the difference between the in-plane and the out-of-plane TMR. This may arise from a tetragonal distortion of the unit cell.

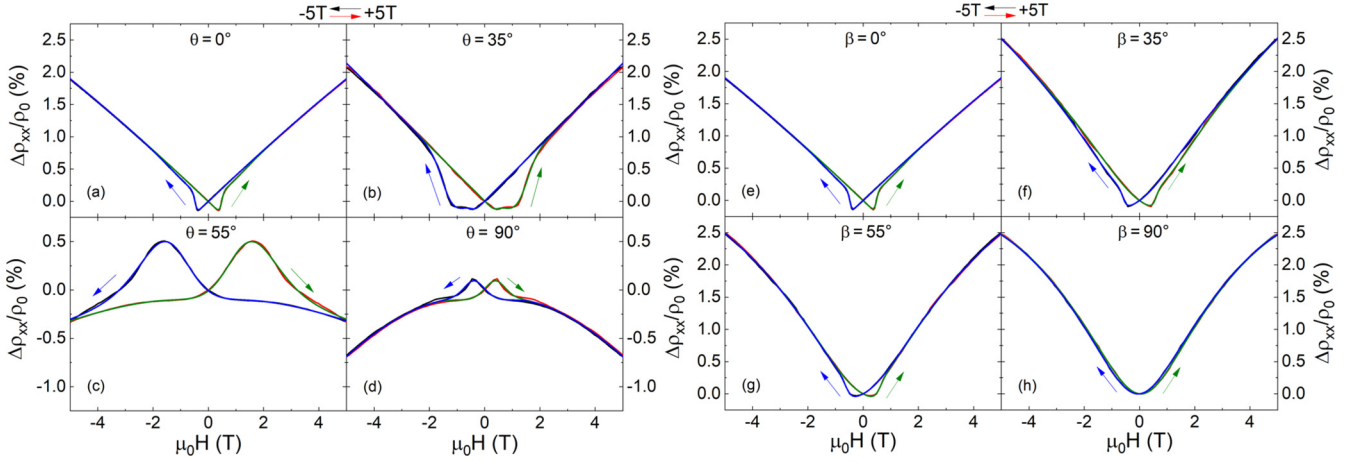


FIG. 16. Angle dependence of magnetoresistance (black and red lines) and two-channel fit (blue and green lines) at 10 K for various tilt angles parallel to the current direction—(a) $\theta = 0^\circ$, (b) $\theta = 35^\circ$, (c) $\theta = 55^\circ$, and (d) $\theta = 90^\circ$ —and perpendicular to the current direction—(e) $\beta = 0^\circ$, (f) $\beta = 35^\circ$, (g) $\beta = 55^\circ$, and (h) $\beta = 90^\circ$.

IV. DISCUSSION AND CONCLUSION

Heterostructures of the bilayer SROSIO with various repetitions were grown on (001)-oriented STO substrates. The strain transfer from the substrate through all layers of the heterostructure was checked by reciprocal space maps around the ($h03$) and ($h04$) substrate peaks (see Fig. 1(c) and Fig. S4 of the Supplemental Material [44]). Comparison of out-of-plane and in-plane magnetization indicates out-of-plane anisotropy. The FM ordering temperature T_C and saturation magnetization for all heterostructures are reduced compared to the pure SRO reference, stronger for fewer bilayer repetitions.

DFT + U + SOC calculations for an $(\text{SRO})_5/(\text{SIO})_2$ SL along [001] confirm the itinerant ferromagnetic state of the ruthenate layers and moderate electronic reconstruction, leading to a negative AHE. They also show the crossing of several bands at the Fermi edge, justifying the application of the phenomenological two-band model for the description of magnetoresistance and Hall effect data.

Hall effect measurements at various temperatures with out-of-plane-oriented magnetic fields show distinct anomalies. Using a two-channel anomalous Hall effect model we found

in our symmetric $[(\text{SrRuO}_3)_5/(\text{SrIrO}_3)_2]_k$ heterostructures that these anomalies do not originate from two independent spin-polarized conduction channels represented by anomalous Hall effects with different signs. Thus, we attribute these additional contributions to the topological Hall effect resulting from skyrmions, in contrast to the asymmetric SrRuO_3 -based heterostructures in [64], for which the total Hall effect could be modeled within the two-channel model. Temperature-dependent magnetoresistance with an out-of-plane-oriented magnetic field displays a crossover upon cooling below 60 K from positive to negative MR. To fit the MR we introduce a two-channel MR model, comparable to the two-channel anomalous Hall effect model with similar coercitive fields.

Angle-dependent Hall effect measurements were performed for tilting the magnetic field from out-of-plane to in-plane, for configurations both perpendicular and parallel to the current j . The ordinary Hall constant R_0 and the shape of the Hall resistance show the same angle dependence for both tilt directions. Adjusting the shape of the Hall effect by the two-channel model we found an additional contribution $\Delta\rho_{\text{Hall}}$ for a large range of magnetic field orientations with

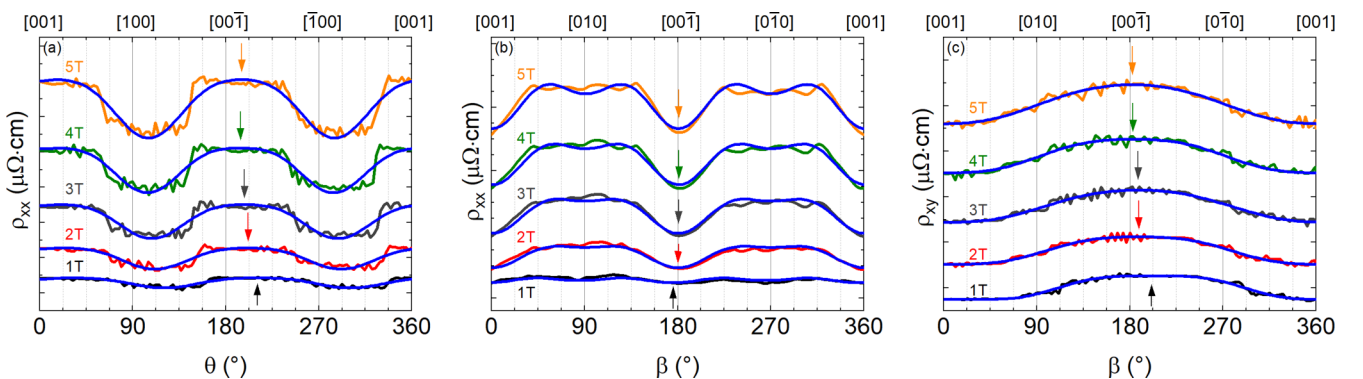


FIG. 17. Angle-dependent magnetoresistance ρ_{xx} (with differing constant offsets for various applied constant magnetic fields) for tilt from the sample normal to the in-plane direction parallel to the current (a) and from the sample normal to the in-plane direction perpendicular to the current (b), as well as Hall resistivity ρ_{xy} for the latter tilt direction (c). Modeling (see the text) is shown by blue lines. Arrows indicate the orientation of the symmetry axes.

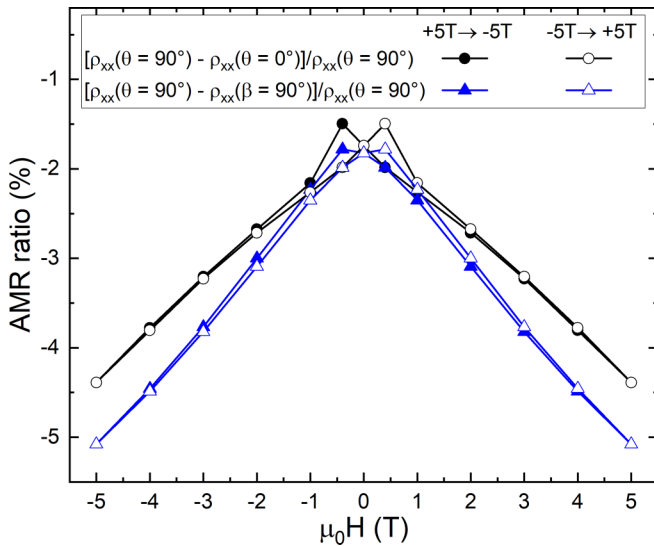


FIG. 18. AMR ratio (out of plane: black lines, in plane: blue lines) of a $[(\text{SRO})_5/(\text{SIO})_2]_{10}$ heterostructure at 10 K.

respect to the film surface. Note that such a $\Delta\rho_{\text{Hall}}$ is not present in pure SRO thin films and therefore must be related to the interfaces in the heterostructures. We interpret it as a THE due to noncoplanar magnetic structures like skyrmions of size $r_{\text{sk}} \approx 20$ nm. Analyzing the field dependence of $\Delta\rho_{\text{Hall}}$ reveals that these skyrmions are only stable for tilting the field from the sample normal to in-plane up to a critical angle of about 45° . Moreover, for field angles close to an in-plane orientation we found a peaklike anomaly in the Hall effect. This could be caused by a nontrivial spin structure different from that of Néel-type skyrmions due to the orientation of the magnetic moments parallel to the film plane. Possible candidates are magnetic bimerons.

To further support the THE origin of $\Delta\rho_{\text{Hall}}$ in our samples we discuss why alternative interpretations are unlikely. For a defect-induced origin of the anomalies in the transverse resistivity (e.g., Ru vacancies [26]) or the existence of different magnetic domains [21] $\Delta\rho_{\text{Hall}}$ reaches its maximum value close to the temperature of the AHE sign change. This is not the case in our thin films [cf. Fig. 9(a)], for which the maximum of the additional contribution occurs at lower temperatures. Manipulation of the magnetic properties of the thin film resulting in a spatial variation of the magnetic and electronic structure is another possible explanation. In a single SRO film this was realized through partial relaxation [22]. Originating from such magnetic inhomogeneities both the shape of ρ_{AHE} and the measured value of $\Delta\rho_{\text{Hall}}$ display a negligible field-angle dependence. In reciprocal space maps of our sample (see Fig. 1(c) here and Fig. S4 of the Supplemental Material [44]) no evidence of structural

relaxation could be observed. Furthermore, both ρ_{AHE} and $\Delta\rho_{\text{Hall}}$ display a strong angular dependence. Therefore the emergence of anomalies in the Hall effect due to a (partial) relaxation-induced inhomogeneous magnetic structure is unlikely. In multilayers based on a symmetric trilayer of SIO (2 u.c.)–SRO (6 u.c.)–SIO (2 u.c.) the formation of skyrmions is unfavorable due to the symmetric boundary conditions in all SRO layers [24]. The magnetization of the heterostructure with several repetitions of the trilayer indicates different Curie temperatures. This was interpreted as a variation of the magnetic properties between individual SRO layers, resulting in different magnetic and electronic structures for each SRO layer. For our $[(\text{SrRuO}_3)_5/(\text{SrIrO}_3)_2]_k$ heterostructures there is no evidence of multiple T_C values in the temperature-dependent magnetization (see the Supplemental Material [44]). Thus, there is no suggestion of an epitaxial strain-induced variation of the magnetic properties of the individual SRO layers. The difference between our bilayer structure SRO (5 u.c.)–SIO (2 u.c.) and the SIO (2 u.c.)–SRO (6 u.c.)–SIO (2 u.c.) trilayer lies in the lower interface of the very first SRO layer, which in our case is between SRO and the STO substrate. Accordingly, the DMI from both interfaces of this layer does not cancel and the skyrmion formation becomes possible.

MR was measured for two tilt directions of the magnetic field, both parallel and perpendicular to the current. At fixed tilt angles the MR undergoes a crossover from positive to negative when the magnetic field is inclined towards the direction of the current, whereas it stays positive for a tilt direction perpendicular to the current.

The anisotropic magnetoresistance is significantly larger (e.g., by about 18% at 5 T) for in-plane compared to out-of-plane orientations, consistent with isofield angular-dependent measurements. The difference between both AMR ratios is related to the difference between in-plane and out-of-plane TMR, which could be caused by the tetragonal distortion of the unit cell. At low fields we observe a rotation of the magnetization direction from the out-of-plane direction which is reversed in larger fields. Altogether, our study on SROSIO heterostructures indicates a modification of the properties of pure SRO by the epitaxial SIO interfaces.

ACKNOWLEDGMENTS

We thank S. Meir and V. Bruchmann-Bamberg for technical support and I. Kézsmárki for useful discussions. This work was supported by the German Research Foundation (DFG) through Projects 107745057 (TRR80) and RO 5387/3-1. We acknowledge computational time at the Leibniz Rechenzentrum Garching (Project pr87ro) and MagnitUDE (DFG Grant No. INST 20876/209-1 FUGG).

- [1] T. H. R. Skyrme, A unified field theory of mesons and baryons, *Nucl. Phys.* **31**, 556 (1962).
- [2] A. Fert, N. Reyren, and V. Cros, Magnetic skyrmions: Advances in physics and potential applications, *Nat. Rev. Mater.* **2**, 17031 (2017).

- [3] G. Finocchio, F. Büttner, R. Tomasello, M. Carpentieri, and M. Kläui, Magnetic skyrmions: From fundamental to applications, *J. Phys. D Appl. Phys.* **49**, 423001 (2016).
- [4] K. Wang, L. Qian, S.-C. Ying, G. Xiao, and X. Wu, Controlled modification of skyrmion information in a

- three-terminal racetrack memory, *Nanoscale* **11**, 6952 (2019).
- [5] N. Nagaosa and Y. Tokura, Topological properties and dynamics of magnetic skyrmions, *Nat. Nanotechnol.* **8**, 899 (2013).
- [6] Y. Li, L. Zhang, Q. Zhang, C. Li, T. Yang, Y. Deng, L. Gu, and D. Wu, Emergent topological Hall effect in $\text{La}_{0.7}\text{Sr}_{0.3}\text{MnO}_3/\text{SrIrO}_3$ heterostructures, *ACS Appl. Mater. Interfaces* **11**, 21268 (2019).
- [7] T. Nan, T. Anderson, J. Gibbons, K. Hwang, N. Campbell, H. Zhou, Y. Dong, G. Kim, D. Shao, T. Paudel, N. Reynolds, X. Wang, N. Sun, E. Tsymbal, S. Choi, M. Rzechowski, Y. B. Kim, D. Ralph, and C. Eom, Anisotropic spin-orbit torque generation in epitaxial SrIrO_3 by symmetry design, *Proc. Natl. Acad. Sci. USA* **116**, 16186 (2019).
- [8] L. Fruchter, O. Schneegans, and Z. Li, Anisotropy and interaction effects of strongly strained SrIrO_3 thin films, *J. Appl. Phys.* **120**, 075307 (2016).
- [9] S. Agrestini, Z. Hu, C.-Y. Kuo, M. W. Haverkort, K.-T. Ko, N. Hollmann, Q. Liu, E. Pellegrin, M. Valvidares, J. Herrero-Martin, P. Gargiani, P. Gegenwart, M. Schneider, S. Esser, A. Tanaka, A. C. Komarek, and L. H. Tjeng, Electronic and spin states of SrRuO_3 thin films: An x-ray magnetic circular dichroism study, *Phys. Rev. B* **91**, 075127 (2015).
- [10] K. Ishigami, K. Yoshimatsu, D. Toyota, M. Takizawa, T. Yoshida, G. Shibata, T. Harano, Y. Takahashi, T. Kadono, V. K. Verma, V. R. Singh, Y. Takeda, T. Okane, Y. Saitoh, H. Yamagami, T. Koide, M. Oshima, H. Kumigashira, and A. Fujimori, Thickness-dependent magnetic properties and strain-induced orbital magnetic moment in SrRuO_3 thin films, *Phys. Rev. B* **92**, 064402 (2015).
- [11] L. Wang, Q. Feng, Y. Kim, R. Kim, K. H. Lee, S. D. Pollard, Y. J. Shin, H. Zhou, W. Peng, D. Lee, W. Meng, H. Yang, J. H. Han, M. Kim, Q. Lu, and T. W. Noh, Ferroelectrically tunable magnetic skyrmions in ultrathin oxide heterostructures, *Nat. Mater.* **17**, 1087 (2018).
- [12] N. Nakagawa, H. Y. Hwang, and D. A. Muller, Why some interfaces cannot be sharp, *Nat. Mater.* **5**, 204 (2006).
- [13] J. Matsuno, N. Ogawa, K. Yasuda, F. Kagawa, W. Koshibae, N. Nagaosa, Y. Tokura, and M. Kawasaki, Interface-driven topological Hall effect in SrRuO_3 - SrIrO_3 bilayer, *Sci. Adv.* **2**, e1600304 (2016).
- [14] K. Everschor-Sitte and M. Sitte, Real-space berry phases: Skyrmion soccer [invited], *J. Appl. Phys.* **115**, 172602 (2014).
- [15] A. Neubauer, C. Pfleiderer, B. Binz, A. Rosch, R. Ritz, P. G. Niklowitz, and P. Böni, Topological Hall Effect in the A Phase of MnSi , *Phys. Rev. Lett.* **102**, 186602 (2009).
- [16] Y. Ohuchi, J. Matsuno, N. Ogawa, Y. Kozuka, M. Uchida, Y. Tokura, and M. Kawasaki, Electric-field control of anomalous and topological Hall effects in oxide bilayer thin films, *Nat. Commun.* **9**, 213 (2018).
- [17] B. Sohn, B. Kim, S. Y. Park, H. Y. Choi, J. Y. Moon, T. Choi, Y. J. Choi, T. W. Noh, H. Zhou, S. H. Chang, J. H. Han, C. Kim, B. Sohn, B. Kim, S. Y. Park, H. Y. Choi, J. Y. Moon, T. Choi, Y. J. Choi, T. W. Noh, H. Zhou, S. H. Chang, J. H. Han, and C. Kim, Emergence of robust 2D skyrmions in SrRuO_3 ultrathin film without the capping layer, [arXiv:1810.01615v1](https://arxiv.org/abs/1810.01615v1).
- [18] C. Wang, C.-H. Chang, A. Herklotz, C. Chen, F. Ganss, U. Kentsch, D. Chen, X. Gao, Y.-J. Zeng, O. Hellwig, M. Helm, S. Gemming, Y.-H. Chu, and S. Zhou, Topological Hall effect in single thick SrRuO_3 layers induced by defect engineering, *Adv. Electron. Mater.* **6**, 2000184 (2020).
- [19] B. Pang, L. Zhang, Y. Chen, J. Zhou, S. Yao, S. Zhang, and Y. Chen, Spin-glass-like behavior and topological Hall effect in $\text{SrRuO}_3/\text{SrIrO}_3$ superlattices for oxide spintronics applications, *ACS Appl. Mater. Interfaces* **9**, 3201 (2017).
- [20] K.-Y. Meng, A. S. Ahmed, M. Baćani, A.-O. Mandru, X. Zhao, N. Bagués, B. D. Esser, J. Flores, D. W. McComb, H. J. Hug, and F. Yang, Observation of nanoscale skyrmions in $\text{SrIrO}_3/\text{SrRuO}_3$ bilayers, *Nano Lett.* **19**, 3169 (2019).
- [21] D. Kan, T. Moriyama, K. Kobayashi, and Y. Shimakawa, Alternative to the topological interpretation of the transverse resistivity anomalies in SrRuO_3 , *Phys. Rev. B* **98**, 180408(R) (2018).
- [22] L. Miao, N. J. Schreiber, H. P. Nair, B. H. Goodge, S. Jiang, J. P. Ruf, Y. Lee, M. Fu, B. Tsang, Y. Li, C. Zeledon, J. Shan, K. F. Mak, L. F. Kourkoutis, D. G. Schlom, and K. M. Shen, Strain relaxation induced transverse resistivity anomalies in SrRuO_3 thin films, *Phys. Rev. B* **102**, 064406 (2020).
- [23] W. Wang, L. Li, J. Liu, B. Chen, Y. Ji, J. Wang, G. Cheng, Y. Lu, G. Rijnders, G. Koster, W. Wu, and Z. Liao, Magnetic domain engineering in SrRuO_3 thin films, *npj Quantum Mater.* **5**, 73 (2020).
- [24] L. Yang, L. Wysocki, J. Schöpf, L. Jin, A. Kovács, F. Gunkel, R. Dittmann, P. H. M. van Loosdrecht, and I. Lindfors-Vrejoiu, Origin of the hump anomalies in the Hall resistance loops of ultrathin $\text{SrRuO}_3/\text{SrIrO}_3$ multilayers, *Phys. Rev. Materials* **5**, 014403 (2021).
- [25] L. Wang, Q. Feng, H. G. Lee, E. K. Ko, Q. Lu, and T. W. Noh, Controllable thickness inhomogeneity and Berry curvature engineering of anomalous Hall effect in SrRuO_3 ultrathin films, *Nano Lett.* **20**, 2468 (2020).
- [26] D. Kan and Y. Shimakawa, Defect-induced anomalous transverse resistivity in an itinerant ferromagnetic oxide, *Phys. Status Solidi B* **255**, 1800175 (2018).
- [27] D. J. Groenendijk, C. Autieri, T. C. van Thiel, W. Brzezicki, J. R. Hortensius, D. Afanasiev, N. Gauquelin, P. Barone, K. H. W. van den Bos, S. van Aert, J. Verbeeck, A. Filippetti, S. Picozzi, M. Cuoco, and A. D. Caviglia, Berry phase engineering at oxide interfaces, *Phys. Rev. Research* **2**, 023404 (2020).
- [28] V. Moshnyaga, I. Khoroshun, A. Sidorenko, P. Petrenko, A. Weidinger, M. Zeitler, B. Rauschenbach, R. Tidecks, and K. Samwer, Preparation of rare-earth manganite-oxide thin films by metalorganic aerosol deposition technique, *Appl. Phys. Lett.* **74**, 2842 (1999).
- [29] M. Schneider, V. Moshnyaga, and P. Gegenwart, Ferromagnetic quantum phase transition in $\text{Sr}_{1-x}\text{Ca}_x\text{RuO}_3$ thin films, *Phys. Status Solidi B* **247**, 577 (2010).
- [30] M. Schneider, D. Geiger, S. Esser, U. S. Pracht, C. Stingl, Y. Tokiwa, V. Moshnyaga, I. Sheikin, J. Mravlje, M. Scheffler, and P. Gegenwart, Low-Energy Electronic Properties of Clean CaRuO_3 : Elusive Landau quasiparticles, *Phys. Rev. Lett.* **112**, 206403 (2014).
- [31] M. Jungbauer, S. Hühn, R. Egoavil, H. Tan, J. Verbeeck, G. Van Tendeloo, and V. Moshnyaga, Atomic layer epitaxy of Ruddlesden-Popper $\text{SrO}(\text{SrTiO}_3)_n$ films by means of metalorganic aerosol deposition, *Appl. Phys. Lett.* **105**, 251603 (2014).
- [32] S. Macke and E. Goering, Magnetic reflectometry of heterostructures, *J. Phys.: Condens. Matter* **26**, 363201 (2014).

- [33] W. Kohn and L. J. Sham, Self-consistent equations including exchange and correlation effects, *Phys. Rev.* **140**, A1133 (1965).
- [34] G. Kresse and J. Furthmüller, Efficient iterative schemes for ab initio total-energy calculations using a plane-wave basis set, *Phys. Rev. B* **54**, 11169 (1996).
- [35] J. P. Perdew, A. Ruzsinszky, G. I. Csonka, O. A. Vydrov, G. E. Scuseria, L. A. Constantin, X. Zhou, and K. Burke, Restoring the Density-Gradient Expansion for Exchange in Solids and Surfaces, *Phys. Rev. Lett.* **100**, 136406 (2008).
- [36] V. N. Staroverov, G. E. Scuseria, J. Tao, and J. P. Perdew, Comparative assessment of a new nonempirical density functional: Molecules and hydrogen-bonded complexes, *J. Chem. Phys.* **119**, 12129 (2003).
- [37] V. N. Staroverov, G. E. Scuseria, J. Tao, and J. P. Perdew, Erratum: Comparative assessment of a new nonempirical density functional: Molecules and hydrogen-bonded complexes, *J. Chem. Phys.* **121**, 11507 (2004).
- [38] S. L. Dudarev, G. A. Botton, S. Y. Savrasov, C. J. Humphreys, and A. P. Sutton, Electron-energy-loss spectra and the structural stability of nickel oxide: An LSDA+U study, *Phys. Rev. B* **57**, 1505 (1998).
- [39] J. M. Rondinelli, N. M. Caffrey, S. Sanvito, and N. A. Spaldin, Electronic properties of bulk and thin film SrRuO₃: Search for the metal-insulator transition, *Phys. Rev. B* **78**, 155107 (2008).
- [40] P. Liu, B. Kim, X.-Q. Chen, D. D. Sarma, G. Kresse, and C. Franchini, Relativistic GW+BSE study of the optical properties of Ruddlesden-Popper iridates, *Phys. Rev. Materials* **2**, 075003 (2018).
- [41] A. A. Mostofi, J. R. Yates, Y.-S. Lee, I. Souza, D. Vanderbilt, and N. Marzari, wannier90: A tool for obtaining maximally-localised wannier functions, *Comput. Phys. Commun.* **178**, 685 (2008).
- [42] C. Jones, P. Battle, P. Lightfoot, and W. Harrison, The structure of SrRuO₃ by time-of-flight neutron powder diffraction, *Acta Cryst. C* **45**, 365 (1989).
- [43] J. Zhao, L. Yang, Y. Yu, F. Li, R. Yu, Z. Fang, L. Chen, and C. Jin, High-pressure synthesis of orthorhombic SrIrO₃ perovskite and its positive magnetoresistance, *J. Appl. Phys.* **103**, 103706 (2008).
- [44] See Supplemental Material at <http://link.aps.org/supplemental/10.1103/PhysRevB.103.214430> for additional information on sample quality and magnetotransport, which includes Refs. [24,27,45–48].
- [45] M. A. L. de la Torre, Z. Sefrioui, D. Arias, M. Varela, J. E. Villegas, C. Ballesteros, C. León, and J. Santamaría, Electron-electron interaction and weak localization effects in badly metallic SrRuO₃, *Phys. Rev. B* **63**, 052403 (2001).
- [46] J. Matsuno, K. Ihara, S. Yamamura, H. Wadati, K. Ishii, V. Shankar, H.-Y. Kee, and H. Takagi, Engineering a Spin-Orbital Magnetic Insulator by Tailoring Superlattices, *Phys. Rev. Lett.* **114**, 247209 (2015).
- [47] M. Srba, Microstructure and electrical transport in Sr_{1-x}Ca_xRuO₃ thin films. The way of revelation of fermi liquid groundstate in CaRuO₃, Ph.D. thesis, Georg-August-Universität Göttingen, 2018.
- [48] T. C. van Thiel, D. J. Groenendijk, and A. D. Caviglia, Extraordinary Hall balance in ultrathin SrRuO₃ bilayers, *J. Phys. Mater.* **3**, 025005 (2020).
- [49] R. M. Azzam, M. Elshazly-Zaghloul, and N. Bashara, Combined reflection and transmission thin-film ellipsometry: A unified linear analysis, *Appl. Opt.* **14**, 1652 (1975).
- [50] M. A. Zeb and H.-Y. Kee, Interplay between spin-orbit coupling and Hubbard interaction in SrIrO₃ and related Pbnm perovskite oxides, *Phys. Rev. B* **86**, 085149 (2012).
- [51] A. Soumyanarayanan, N. Reyren, A. Fert, and C. Panagopoulos, Emergent phenomena induced by spinorbit coupling at surfaces and interfaces, *Nature* **539**, 509 (2016).
- [52] J. Cho, N.-H. Kim, S. Lee, J.-S. Kim, R. Lavrijsen, A. Solignac, Y. Yin, D.-S. Han, N. J. Van Hoof, H. J. Swagten, B. Koopmans, and C.-Y. You, Thickness dependence of the interfacial Dzyaloshinskii-Moriya interaction in inversion symmetry broken systems, *Nat. Commun.* **6**, 7635 (2015).
- [53] N. Haham, Y. Spherber, M. Schultz, N. Naftalis, E. Shimshoni, J. W. Reiner, and L. Klein, Scaling of the anomalous Hall effect in SrRuO₃, *Phys. Rev. B* **84**, 174439 (2011).
- [54] G. Kim, K. Son, Y. E. Suyolcu, L. Miao, N. J. Schreiber, H. P. Nair, D. Putzky, M. Minola, G. Christiani, P. A. van Aken, K. M. Shen, D. G. Schlom, G. Logvenov, and B. Keimer, Inhomogeneous ferromagnetism mimics signatures of the topological hall effect in SrRuO₃ films, *Phys. Rev. Materials* **4**, 104410 (2020).
- [55] T. Yokouchi, N. Kanazawa, A. Tsukazaki, Y. Kozuka, M. Kawasaki, M. Ichikawa, F. Kagawa, and Y. Tokura, Stability of two-dimensional skyrmions in thin films of Mn_{1-x}Fe_xSi investigated by the topological Hall effect, *Phys. Rev. B* **89**, 064416 (2014).
- [56] A. O. Leonov and I. Kézsmárki, Skyrmion robustness in non-centrosymmetric magnets with axial symmetry: The role of anisotropy and tilted magnetic fields, *Phys. Rev. B* **96**, 214413 (2017).
- [57] K.-W. Moon, J. Yoon, C. Kim, and C. Hwang, Existence of In-Plane Magnetic Skyrmion and its Motion Under Current Flow, *Phys. Rev. Appl.* **12**, 064054 (2019).
- [58] B. Göbel, A. Mook, J. Henk, I. Mertig, and O. A. Tretiakov, Magnetic bimerons as skyrmion analogues in in-plane magnets, *Phys. Rev. B* **99**, 060407(R) (2019).
- [59] P. Zhang, A. Das, E. Barts, M. Azhar, L. Si, K. Held, M. Mostovoy, and T. Banerjee, Robust skyrmion-bubble textures in SrRuO₃ thin films stabilized by magnetic anisotropy, *Phys. Rev. Research* **2**, 032026(R) (2020).
- [60] K. Takiguchi, Y. K. Wakabayashi, H. Irie, Y. Krockenberger, T. Otsuka, H. Sawada, M. Tanaka, Y. Taniyasu, and H. Yamamoto, Emergence of Weyl fermions in an epitaxial ferromagnetic oxide, *Nat. Commun.* **11**, 4969 (2020).
- [61] J. Xu, M. K. Ma, M. Sultanov, Z.-L. Xiao, Y.-L. Wang, D. Jin, Y.-Y. Lyu, W. Zhang, L. N. Pfeiffer, K. W. West, K. W. Baldwin, M. Shayegan, and W.-K. Kwok, Negative longitudinal magnetoresistance in gallium arsenide quantum wells, *Nat. Commun.* **10**, 287 (2019).
- [62] W. Limmer, J. Daeubler, L. Dreher, M. Glunk, W. Schoch, S. Schwaiger, and R. Sauer, Advanced resistivity model for arbitrary magnetization orientation applied to a series of compressive- to tensile-strained (Ga,Mn)As layers, *Phys. Rev. B* **77**, 205210 (2008).
- [63] W. Limmer, M. Glunk, J. Daeubler, T. Hummel, W. Schoch, R. Sauer, C. Bihler, H. Huebl, M. S. Brandt, and S. T. B. Goennenwein, Angle-dependent magnetotransport in cubic and tetragonal ferromagnets: Application to (001)-

- and(113)A-oriented(Ga,Mn)As, [Phys. Rev. B **74**, 205205 \(2006\)](#).
- [64] L. Wysocki, J. Schöpf, M. Ziese, L. Yang, A. Kovács, L. Jin, R. B. Versteeg, A. Bliesener, F. Gunkel, L. Kornblum, R. Dittmann, P. H. M. van Loosdrecht, and I. Lindfors-Vrejoiu, Electronic inhomogeneity influence on the anomalous Hall resistivity loops of SrRuO₃ epitaxially interfaced with 5d perovskites, [ACS Omega **5**, 5824 \(2020\)](#).